# Optimal method for exoplanet detection by angular differential imaging

**Laurent M. Mugnier,[1,2,*] Alberto Cornia,[1,2,3] Jean-François Sauvage,[1,3] Gérard Rousset,[2,3] Thierry Fusco,[1,3] and Nicolas Védrenne[1,3]**

[1]*ONERA/DOTA (Département d'Optique Théorique et Appliquée), B.P. 72, 92322 Châtillon cedex, France*
[2]*LESIA (Laboratoire d'Etudes des Systemes Informatiques et Automatiques), Observatoire de Paris, 5 place Jules Janssen, 92195 Meudon, France*
[3]*Groupement d'Intérêt Scientifique PHASE (Partenariat Haute résolution Angulaire Sol Espace) between ONERA, Observatoire de Paris, CNRS, and Université Paris Diderot*
**Corresponding author: mugnier@onera.fr*

Received September 16, 2008; revised February 13, 2009; accepted March 24, 2009; posted April 9, 2009 (Doc. ID 101668); published May 12, 2009

We propose a novel method for the efficient direct detection of exoplanets from the ground using angular differential imaging. The method combines images appropriately, then uses the combined images jointly in a maximum-likelihood framework to estimate the position and intensity of potential planets orbiting the observed star. It takes into account the mixture of photon and detector noises and a positivity constraint on the planet's intensity. A reasonable detection criterion is also proposed based on the computation of the noise propagation from the images to the estimated intensity of the potential planet. The implementation of this method is tested on simulated data that take into account static aberrations before and after the coronagraph, residual turbulence after adaptive optics correction, and noise. 

*OCIS codes:* 100.3190, 110.3010, 110.2970, 110.1080.

## 1. INTRODUCTION

The direct detection of exoplanets from the ground is a very promising field of astronomy today [1]. A goal is the characterization of the physical composition of the exoplanets by a spectral analysis of their emitted and/or reflected light. This observation from the ground is a technological challenge. Indeed, in order to be able to observe a sufficient number of targets, it is required to cope with an intensity ratio (also called contrast) between the star and its planet that may be as high as $10^6$ in IR bands [2] at very small angular separations. Two consortia are currently building planet searchers based on direct imaging in the near-IR: SPHERE (Spectro-Polarimetry High-contrast Exoplanet Research) [3] for the Very Large Telescope of the European Southern Observatory (VLT) (ESO) and GPI (Gemini Planet Imager) [4] for GEMINI observatory. The goal of the European project SPHERE is to detect giant planets orbiting nearby stars up to 100 pc from the Sun. For instance these planets may present an atmosphere rich in methane [5], with interesting spectral signatures around 1.6 $\mu$m to be used in spectral imaging. The planets searched for have orbits typically between 5 and 100 astronomical units. This requires being able to resolve an angular separation between the planet and its parent star that can be as small as a few diffraction elements ($\lambda/D$).

The SPHERE instrument is a combination of several optical features, all of them optimized toward the final goal of exoplanet detection. First of all, an extreme adaptive optics system (XAO) concentrates the light into a coherent Airy pattern, performing a real-time correction of Earth's atmospheric turbulence [6]. Then, the coronagraphic stage strongly attenuates the star intensity and therefore significantly reduces the photon noise. The coronagraphs considered in the SPHERE project are a Lyot coronagraph [7], a four-quadrant phase mask [8], and an apodized Lyot coronagraph [9].

The final optical quality is a key factor in direct exoplanet detection, because the main limitation for the detection of faint objects is demonstrated to be the static speckles in the coronagraphic images of the star [10]. These speckles are the consequence of an imperfect correction of static aberrations before the coronagraph. Note that because we are dealing with long-exposure images, the turbulence residuals are averaged and form a halo around the position of the star in the focal plane; the speckles are due only to static aberrations.

The combination of XAO and a coronagraphic device is necessary to reduce both photon noise and speckle in the final image, but is not sufficient for the considered intensity ratios between star and planet. To attain the detection performance needed to detect a large number of planets, it is mandatory to combine the above-mentioned optical devices with an *a posteriori* processing of all the data. The main problem is to disentangle the potential planet signal from the quasi-static speckles, that are due to static aberrations and constitute a major noise source. These speckles present the same characteristic angular size as the planet signal $\lambda/D$. With no more information, it is impossible to discriminate between the speckles and the planet. In order to do so, the SPHERE instrument includes the ability to perform spectral and angular differential imaging.

Spectral differential imaging consists of acquiring si-

 

multaneous images of the star–planet system at different wavelengths [11,12]. The spectral signature of the exoplanet's atmosphere ensures that the planet signal will significantly vary between spectral images taken in two slightly different spectral bands, while the star signal and therefore the speckles remain the same. A subtraction of two such images brings a significant attenuation of the star signal while enhancing the planet signal. With the IRDIS (Infra-Red Dual-beam Imaging and Spectroscopy) instrument [13] of SPHERE, one can make use of two close spectral channels, e.g., between bands $H2=1.59$ $\mu$m and $H3=1.64$ $\mu$m, the latter corresponding to a methane absorption line.

Angular differential imaging is a method originally designed for the calibration of static speckles for the Hubble Space Telescope—see, e.g., [14,15] and references therein. The original idea was to perform a rotation of the entire telescope, and therefore of the observed field on the detector, while the telescope point-spread function (PSF), which is the star signal and includes the static speckles, would remain the same. This idea has been developed recently in the case of a ground-based observation [16,17].

For instance at the Nasmyth foci of an alt–az mount telescope, both field and pupil rotate during the tracking of the target in the sky. The observer has the choice of implementing a de-rotation of the field image or of the pupil one. For angular differential imaging, we choose a de-rotation of the pupil image, thus ensuring the best temporal stability of the quasi-static speckles. In an image series obtained in these conditions with the star on-axis, the additional information we have at hand is therefore the induced circular trajectory of the planet through the images of the series.

In Section 2, we present our processing method, which aims at exploiting the field rotation in a ground-based imager dedicated to exoplanet detection. Note that the method could actually also be used to detect weak companion stars. The estimation of the planet position and intensity is done on the differential data, through a maximum-likelihood approach as presented in Section 3. An associated detection criterion is proposed in Section 4, and the complete method is tested in Section 5. Section 6 concludes the paper.

## 2. PRINCIPLE OF THE PROPOSED METHOD

If both angular and spectral data are available, as is the case with the SPHERE instrument, then one may first combine each pair of simultaneous spectral images into one image so as to enhance the planet signal by a partial suppression of the static speckles of the star signal, and then use the resulting combined image series as angular data.

In this paper, we do not consider that we record simultaneous spectral images. We assume that we have a series of angular images, and we investigate their joint processing. These images correspond to different recording times and therefore to different positions of the planet signal in the focal plane due to the field rotation. At least two approaches are possible for this problem:

- jointly estimate the star signal (coronagraphic response in our case) and the planet position and intensity [18,19] from the angular image series;
- first, subtract two by two the angular images to remove the star signal (the speckles) and produce angular differential data; second, estimate the planet [20,21] only from this new angular differential data series.

In the framework of the SPHERE project, the static aberrations are likely to slowly evolve during observing time, and if the first option above were chosen, the estimation of the star signal should therefore be done several times during the night. We therefore choose the second option, which consists of removing the star signal numerically by performing an angular image subtraction between image pairs taken at time intervals that are long enough to obtain the peculiar signature of the planet's apparent rotation but shorter than the evolution time of the static aberrations. This signature is illustrated in Fig. 1. Let $\boldsymbol{i}_t$ be the raw image at time $t$; the new data are image differences $\Delta(\boldsymbol{r},t_1,t_2)$:

$$\Delta(\boldsymbol{r},t_1,t_2) \triangleq \boldsymbol{i}_{t_1}(\boldsymbol{r}) - \boldsymbol{i}_{t_2}(\boldsymbol{r}), \tag{1}$$

where $t_1$ and $t_2$ are chosen times and $\boldsymbol{r}$ the position in the focal plane.

In the angular image series, there is a very large number of possible couples $(t_1,t_2)$. In this paper, we select the time couples so that (a) all images are selected at least

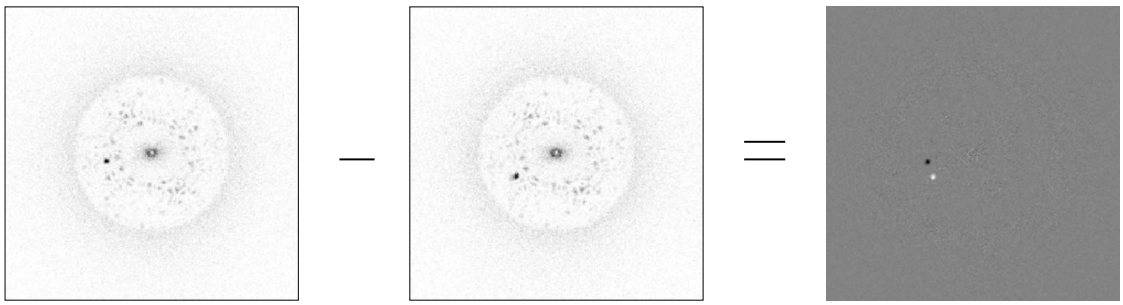

Fig. 1. Illustration of the angular differences performed on the raw data. Left and center: two noiseless raw coronagraphic images $\boldsymbol{i}_{t_1}$ and $\boldsymbol{i}_{t_2}$ of a star with a very bright planet ($10^3$ intensity ratio between star and planet). Right: difference $\Delta(\boldsymbol{r},t_1,t_2)$, used as our new data, which completely removes the star signal in this case where the quasi-static aberrations have not evolved. The colormap is inverted for better legibility, with black corresponding to the maximum value.

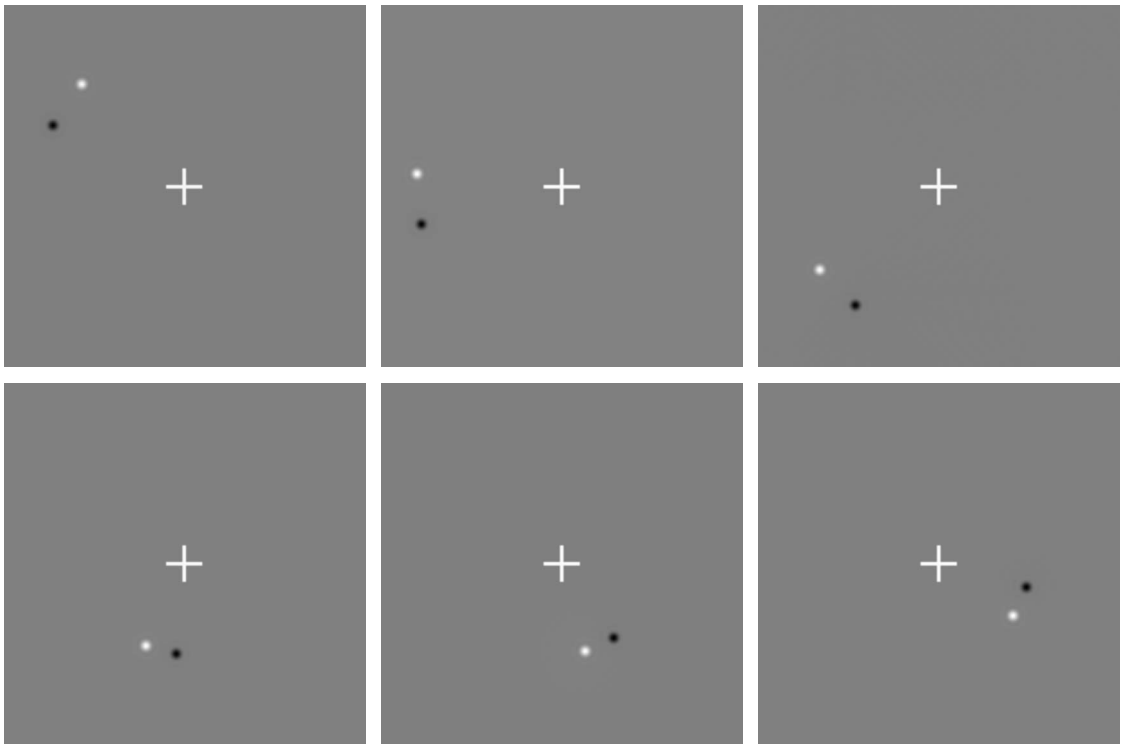

Fig. 2. Examples of planet signatures $\boldsymbol{p}(\boldsymbol{r},k;\boldsymbol{r}_0)$. Top: for one value of $\boldsymbol{r}_0$ and three values of the time index $k$. Bottom: for another value of $\boldsymbol{r}_0$ and the three same values of the time index $k$. The cross in the middle represents the center of the field rotation.

once, (b) at least 95% of the planet signal is preserved in the image difference (which can be shown to imply that the planet must have moved by at least $1.5\lambda/D$), and (c) if possible, the static aberrations are very similar in the two subtracted images. Note that the best compromise may be difficult to achieve because it depends on many factors, i.e., both system parameters, such as the evolution rate of static aberrations, and observational parameters, such as the field rotation speed. In any case, a set of new data are computed using all the raw images. These new data are the ones to be used subsequently to detect the planet(s).

The new data consist of $k_{\max}$ image differences denoted by $\Delta(\boldsymbol{r},k)$, where $k$ is an index used to reference the time couples, and is referred to as the time index in the sequel. Assuming that a planet is present, the data model at each pixel $\boldsymbol{r}$ of image difference $k$ is

$$\Delta(\boldsymbol{r},k) = a\boldsymbol{p}(\boldsymbol{r},k;\boldsymbol{r}_0) + \boldsymbol{n}(\boldsymbol{r},k), \tag{2}$$

where scalar $a$ is the unknown planet intensity, the two-component vector $\boldsymbol{r}_0$ is the unknown planet position at the beginning of the observation (in the first image of the series), $\boldsymbol{n}(\boldsymbol{r},k)$ denotes the noise, and $\boldsymbol{p}(\boldsymbol{r},k;\boldsymbol{r}_0)$ is a synthetic (i.e., noiseless) pattern, which is the precomputed theoretical planet signature (PS) for a planet at an assumed $\boldsymbol{r}_0$ initial position.

The PS of index $k$ is simply the difference of two theoretical noiseless planet images (i.e., PSFs) suitably positioned in the field and corresponding to the field rotations at the two times $t_1$ and $t_2$ used in $\Delta(\boldsymbol{r},k)$. It can be seen as the space- and time-varying PSF of our new data $\Delta(\boldsymbol{r},k)$. It is important to emphasize that the PS directly depends on $\boldsymbol{r}_0$; therefore, a set of PSs must be computed for all the candidate positions of a planet in order to be used later in the detection method. Figure 2 shows such PSs $\boldsymbol{p}(\boldsymbol{r},k;\boldsymbol{r}_0)$ for two different initial positions $\boldsymbol{r}_0$ and three values of the time index $k$.

## 3. MAXIMUM-LIKELIHOOD ESTIMATION FOR POSITION AND INTENSITY OF THE PLANET

The maximum-likelihood approach consists of searching for $(\hat{\boldsymbol{r}}_0,\hat{a})$ that maximize the likelihood $L(\boldsymbol{r}_0,a)$. In the following we assume that the noise is non-homogeneous (i.e., non-stationary), Gaussian, white in both time $k$ and in space $\boldsymbol{r}$, and with variance $\sigma^2(\boldsymbol{r},k)$. This assumption is reasonable and allows us to take into account both the photon and the detector noise, as is done in AO-corrected image restoration [22]: for the intensity levels considered here, the Poisson statistics of photon noise is well approximated by a Gaussian probability density. Its variance map is estimated from the set of images, e.g., as an empirical variance of the image series at each pixel, and is considered known in the following expressions. As for the detector read-out noise, it is reasonably homogeneous white Gaussian and its variance can be estimated beforehand.

The likelihood is given by

$$L(\boldsymbol{r}_0,a) \propto \exp\left\{-\frac{1}{2}\sum_k \sum_{\boldsymbol{r}} \frac{|\Delta(\boldsymbol{r},k) - ap(\boldsymbol{r},k;\boldsymbol{r}_0)|^2}{2\sigma^2(\boldsymbol{r},k)}\right\}. \tag{3}$$

Maximizing this likelihood with respect to $(\boldsymbol{r}_0,a)$ is equivalent to maximizing the following metric, which is equal to the log-likelihood up to unimportant constants:

$$J(\boldsymbol{r}_0,a) \triangleq -a^2\sum_{k,\boldsymbol{r}}\frac{p^2(\boldsymbol{r},k;\boldsymbol{r}_0)}{\sigma^2(\boldsymbol{r},k)} + 2a\sum_{k,\boldsymbol{r}}\frac{p(\boldsymbol{r},k;\boldsymbol{r}_0)\Delta(\boldsymbol{r},k)}{\sigma^2(\boldsymbol{r},k)} \tag{4}$$

$$= 2\ln L(\boldsymbol{r}_0,a) + \text{const.} \tag{5}$$

The optimal value $\hat{a}(\boldsymbol{r}_0)$ of $a$ for each given $\boldsymbol{r}_0$ is computable analytically:

$$\hat{a}(\boldsymbol{r}_0) = \frac{\sum_{k,\boldsymbol{r}} p(\boldsymbol{r},k;\boldsymbol{r}_0)\Delta(\boldsymbol{r},k)/\sigma^2(\boldsymbol{r},k)}{\sum_{k,\boldsymbol{r}} p^2(\boldsymbol{r},k;\boldsymbol{r}_0)/\sigma^2(\boldsymbol{r},k)}. \tag{6}$$

The numerator of this expression can be seen as a scalar product (correlation) between the PS $\boldsymbol{p}(\boldsymbol{r},k;\boldsymbol{r}_0)$ and the image differences $\Delta(\boldsymbol{r},k)$, with weights given by the noise variance. The denominator is simply a normalization constant.

If we insert this optimal value for the intensity into metric $J$, we obtain an expression of the latter that depends, explicitly at least, only on the sought planet position:

$$J'(\boldsymbol{r}_0) \triangleq J[\boldsymbol{r}_0,\hat{a}(\boldsymbol{r}_0)] = \frac{\left[\sum_{k,\boldsymbol{r}} p(\boldsymbol{r},k;\boldsymbol{r}_0)\Delta(\boldsymbol{r},k)/\sigma^2(\boldsymbol{r},k)\right]^2}{\sum_{k,\boldsymbol{r}} p^2(\boldsymbol{r},k;\boldsymbol{r}_0)/\sigma^2(\boldsymbol{r},k)}. \tag{7}$$

This criterion $J'$ can be computed for each possible initial planet position on a grid that can be chosen as the original pixel grid of the images or as a finer grid if it is useful. The most likely initial planet position is then $\hat{\boldsymbol{r}}_0 = \arg\min J'(\boldsymbol{r}_0)$, and the most likely intensity is $\hat{a}(\hat{\boldsymbol{r}}_0)$ as computed with Eq. (6).

This estimator can be improved by constraining the estimated intensity to be positive. Indeed, the value of $\hat{a}(\boldsymbol{r}_0)$ of Eq. (6) is not necessarily positive, whereas the true intensity is. Additionally, because the estimation of $\hat{a}(\boldsymbol{r}_0)$ is a one-dimensional optimization, the optimal intensity subject to the positivity constraint is simply

$$\hat{a}_{pos}(\boldsymbol{r}_0) = \max\{\hat{a}(\boldsymbol{r}_0),0\}. \tag{8}$$

If we now insert this value for the planet intensity into metric $J$, it is easy to show that we obtain the criterion

$$J''(\boldsymbol{r}_0) \triangleq J[\boldsymbol{r}_0,\hat{a}_{pos}(\boldsymbol{r}_0)] = \begin{cases} J'(\boldsymbol{r}_0), & \text{if } \hat{a}(\boldsymbol{r}_0) > 0 \\ 0, & \text{if } \hat{a}(\boldsymbol{r}_0) \leqslant 0 \end{cases}, \tag{9}$$

where $\hat{a}(\boldsymbol{r}_0)$ is given by Eq. (6) and $J'(\boldsymbol{r}_0)$ by Eq. (7).

Figures 3 and 4 illustrate the usefulness of the positivity constraint in the idealized case of a noiseless image: the left and right images of Fig. 3 show the maps $\hat{a}(\boldsymbol{r}_0)$ and $\hat{a}_{pos}(\boldsymbol{r}_0)$, respectively. These maps are the planet intensity estimated at each position $\boldsymbol{r}_0$ without and with the positivity constraint, respectively. In the case without positivity the map is very similar to the auto-correlation of the PS, which explains its shape with two negative bumps. Figure 4 shows the corresponding maps $J'(\boldsymbol{r}_0)$ and $J''(\boldsymbol{r}_0)$ of the log-likelihood obtained, respectively, without [Equation (7)] and with [Equation (9)] the positivity constraint on the intensity. Clearly, $J''$ is very different from a thresholded version of $J'$ and has fewer local maxima: the positivity constraint removes the sidelobes of the log-likelihood, and hence it should contribute to removing false detections in a noisier case.

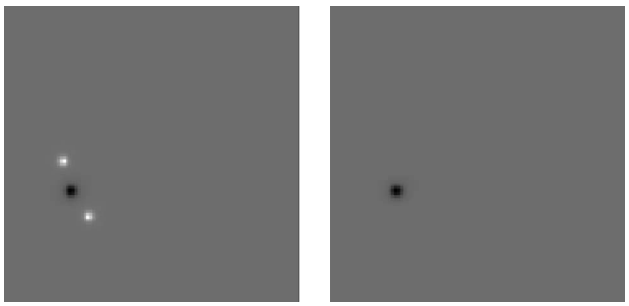

Fig. 3. Intensity maps $\hat{a}(\boldsymbol{r}_0)$ and $\hat{a}_{pos}(\boldsymbol{r}_0)$ estimated without (left) and with (right) the positivity constraint, respectively, in a noiseless case. The colormap is inverted for better legibility: the white sidelobes have the lowest, and negative, value; the gray background has zero value, and black corresponds to the highest value.

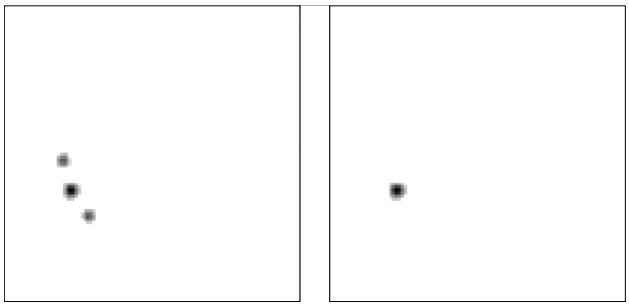

Fig. 4. Log-likelihood maps of the position of the planet in the noiseless case of Fig. 3 without [$J'(\boldsymbol{r}_0)$, left] and with [$J''(\boldsymbol{r}_0)$, right] the positivity constraint on the estimated intensity. The colormap is inverted for better legibility: white is the lowest, and zero, value; black corresponds to the highest value.

## 4. DETECTION CRITERION

Once the likelihood and intensity maps are computed, the main problem is to decide which peaks are true planets and which ones are not. One way to do so is to additionally compute the standard deviation of the estimated intensity $\sigma[\hat{a}(\boldsymbol{r}_0)]$ for each possible planet position $\boldsymbol{r}_0$, i.e., to compute how the noise propagates from the images to our intensity estimator.

We define the signal-to-noise ratio (SNR) of the estimated planet intensity as

$$\text{SNR}[\hat{a}(\boldsymbol{r}_0)] \triangleq \hat{a}(\boldsymbol{r}_0)/\sigma[\hat{a}(\boldsymbol{r}_0)]. \tag{10}$$

A possible detection criterion is then to decide that all positions where this SNR is greater than some threshold are true detections. In the Gaussian setting assumed in this paper, this detection criterion can be linked to the probability of false alarm.

The variance of the estimated intensity for a given position $\boldsymbol{r}_0$ is computed by means of Eq. (6) using the abovementioned property that the noise in our images $\Delta(k,\boldsymbol{r})$ is white, both temporally and spatially:

$$\sigma^2[\hat{a}(\boldsymbol{r}_0)] = \frac{1}{\left[\sum_{\boldsymbol{r}',k'} \frac{p^2(\boldsymbol{r},k';\boldsymbol{r}_0)}{\sigma^2(\boldsymbol{r},k')}\right]^2} \sum_{\boldsymbol{r},k} \left[\frac{p(\boldsymbol{r},k;\boldsymbol{r}_0)}{\sigma^2(\boldsymbol{r},k)}\right]^2 \sigma^2(\boldsymbol{r},k),$$

which can be simplified into

$$\sigma^2[\hat{a}(\boldsymbol{r}_0)] = \left[\sum_{\boldsymbol{r},k} \frac{p^2(\boldsymbol{r},k;\boldsymbol{r}_0)}{\sigma^2(\boldsymbol{r},k)}\right]^{-1}. \quad (11)$$

Interestingly, the SNR of the estimated intensity is linked very directly to the log-likelihood $J'$ of Eq. (7):

$$J'(\boldsymbol{r}_0) = \{\hat{a}(\boldsymbol{r}_0)/\sigma[\hat{a}(\boldsymbol{r}_0)]\}^2 = \{\mathrm{SNR}[\hat{a}(\boldsymbol{r}_0)]\}^2. \quad (12)$$

Consequently, maximizing (resp. thresholding) the likelihood is actually equivalent to maximizing (resp. thresholding) the SNR of the estimated intensity.

*Implementation details*. The computation of the estimated intensity maps and of the likelihood maps is quite straightforward. It is performed by means of Eqs. (6)–(9). The main burden lies in the computation of the PSs $p(\boldsymbol{r},k;\boldsymbol{r}_0)$ for all time indices $k$ and all searched initial planet positions $\boldsymbol{r}_0$. Each of these PSs is the difference of two theoretical noiseless planet images that must be suitably positioned in the field. This requires shifting each of these two theoretical planet images by a non-integer amount, whereas only integer shifts can be performed at very low computational cost. To solve this problem, we pre-compute a library of all the possible shifted theoretical planet images for $x$ and $y$ shifts regularly spaced between zero and one, typically every 1/20th of a pixel. This notably alleviates the computational burden. The total computing time currently remains of the order of three hours for the simulations presented below, which involve a hundred $256\times256$ images and a $200\times200$ grid for the planet position search.

## 5. TESTS ON SIMULATED DATA

### A. Simulation Conditions

We use a Fourier-based simulation method that describes the AO via the spatial power spectrum of the residual phase [23] and is presented in [24]. It takes the following set of parameters, which are representative of the SPHERE/IRDIS instrument on the VLT:

- an 8 m telescope, a seeing of 0.8″, and a wind speed of 12.5 m/s;
- a SAXO-like AO system [6]: $41\times41$ actuators, a $40\times40$ sub-aperture Hartmann–Shack wavefront sensor, a sampling frequency of 1200 Hz;
- static aberrations with a standard deviation of $\sigma_{\phi_u}=35$ nm upstream of the coronagraph and $\sigma_{\phi_d}=100$ nm downstream of the coronagraph. We have assumed a pupil-stabilized mode with static aberrations kept constant during the simulated run.

A hundred $256\times256$ images are simulated at an imaging wavelength of $\lambda=1.593$ $\mu$m with Poisson noise. The image sampling corresponds to that of the SPHERE/IRDIS instrument, which is Shannon-sampled for a wavelength of 0.95 $\mu$m; the images are thus oversampled by a factor $1.593/0.95=1.677$, and their field is $76\lambda/D$ wide. The image of the star is computed by means of the analytical expression for the long-exposure AO-corrected coronagraphic image of a star [25] and is shown on the left part of Fig. 5.

We have simulated seven planets which lie aligned at distances that are multiples of $4\lambda/D$ from the central star. The long-exposure AO-corrected image of a planet is computed using the static aberrations and the phase structure function of the AO-corrected residual phase, assuming that the planets do not "see" the coronagraph. Such an image is presented on the right part of Fig. 5. For each of the seven simulated planets, this long-exposure planet image is then added to each of the star images at the appropriate planet locations. With the currently foreseen integration time of SPHERE/IRDIS images, the smearing of a planet due to field rotation during an individual exposure remains negligible, even for planets far from their star, and is thus not taken into account in the simulation.

The star intensity at the entrance aperture of the telescope is $2.67\times10^7$ ph/s and the planet intensity is 28.5 ph/s; the intensity ratio is thus $9.36\times10^5$. The telescope+instrument transmission is 0.09 without the coronagraph. The coronagraph further attenuates the star light with a transmission factor of 0.13. Depending on the simulation data, the total exposure time is either 1 or 2 h. In the 1 h case the total star intensity is $1.127\times10^7$ ph/image (or 172 ph/pixel on average). The total planet intensity is 93 ph/image in any of the 100 images. This corresponds to a maximum planet intensity of $\simeq$4.8 ph/pixel, the exact maximum value depending on whether or not the planet falls at the center of a pixel in the image.

For the purpose of testing our method, we have simulated the field rotation in the following simplified way:

- 50 images are simulated before the star crosses the meridian, and 50 images afterward; the set of 100 parallactic angles of the star is centered on the meridian.
- The step between two consecutive images is constant; for 100 images it is 1°.
- There is a gap of 20° around the meridian, to prevent the overlapping of the planet signals of two images that are to be subtracted. As a result, the angle between the first and the last image is 120°.

The image combination scheme we chose in these simulations is to associate each image with its symmetrical

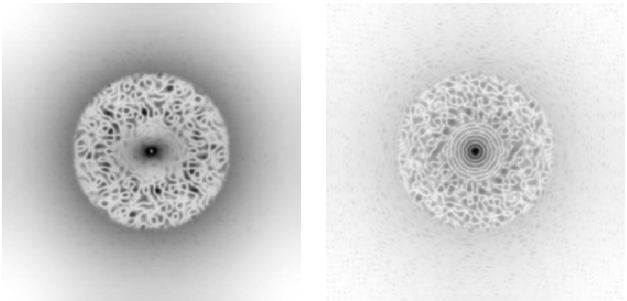

Fig. 5. Simulated PSFs with (left) and without (right) coronagraph in logarithmic scale. Note that for legibility the colormap is inverted, and each of these two images is represented with its own gray-level scale (with black corresponding to its maximum value).

one with respect to the meridian (the first image with the last, the second with the last-but-one, etc.). This way, the position of the achromatic dispersion compensator of the AO system is the same in the two images of each image couple, which should minimize the differential aberrations if the achromatic dispersion compensator is the main contributor to the evolution of the static aberrations.

### B. Impact of the Proposed Positivity Constraint and of the Noise Variance Map

Figure 6 shows the likelihood maps obtained with 100 images and an exposure time of 1 h, with and without the positivity constraint and the non-homogeneous noise variance. The use of a noise variance map can be seen as taking into account some prior knowledge: if the noise variance map is unknown, one will use a homogeneous (i.e., constant) noise variance map, which cancels out in all the above expressions. As can be seen in Fig. 6, the positivity constraint on the planet's intensity and the use of a noise variance map both improve the likelihood map and thus the detection: going from the homogeneous noise variance without positivity (top left) to the homogeneous noise variance with positivity (top right) notably decreases low-level peaks of the likelihood as well as some high-level peaks that correspond to false alarms (for instance, one in the middle, below the center of the image). These are the peaks due to the negative values of the estimated intensity.

Additionally, going from the homogeneous noise variance with positivity (top right) to the inhomogeneous noise variance with positivity (bottom right) further improves the likelihood map by dimming some other spurious peaks (for instance, one on the top left part of the image, at about 45° from the star).

To better quantify the improvement brought by positivity and by the use of an inhomogeneous noise variance map, Fig. 7 shows the SNR of the estimated intensity [defined by Equation (10)] thresholded to values from 3 to 6, in the photon-starved case of a 1 h total observation time. In the two cases where a homogeneous noise is assumed in the processing, the noise variance has been taken equal to the spatial average of the empirical variance of each pixel in time.

As seen on the first two lines of images of Fig. 7, the use of the positivity constraint removes a very substantial number of false alarms. On the same images, one notes that the inhomogeneous noise model also reduces the false alarm rate.

For the case where both the positivity and the inhomo-

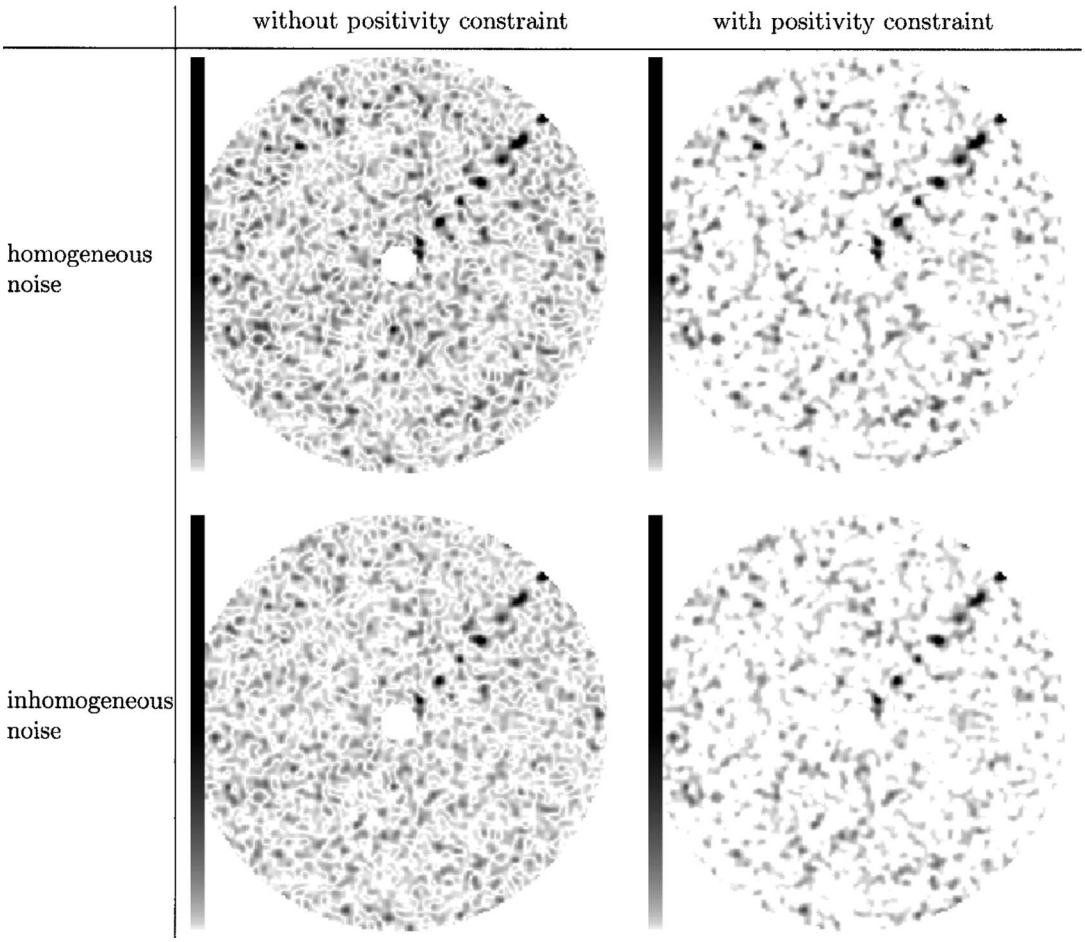


Fig. 6. Likelihood maps with 100 images and an exposure time of 1 h. Top row: homogeneous noise. Bottom row: inhomogeneous noise. Left column: without positivity constraint. Right column: with positivity constraint. For legibility the colormap is inverted: white corresponds to the minimum value of zero, and black to the highest value.

geneous noise variance map are used, there exists in this simulation a threshold (of 4) for which all the true planets are detected and no false alarm is present. The corresponding detection map is the boxed one of Fig. 7. The image immediately on the left, obtained without the positivity constraint, has a false alarm at the very right of the field.

For the three other cases, whatever the chosen threshold, in this simulation there are either false alarms (for low threshold values) or undetected planets (for high threshold values).

One can also note that in the homogeneous cases there are more detected planets for high threshold values, as well as more false alarms for low threshold values, compared to the inhomogeneous cases. For instance, five planets are detected in the homogeneous case with positivity and a $6\sigma$ detection (i.e., a threshold of 6) and only three in the inhomogeneous case. To detect the same number of planets in the inhomogeneous case one must set the threshold to 5 instead of 6. The homogeneous detection maps thus appear to be, so to speak, shifted toward the high thresholds. We conjecture that this is due to the noise standard deviation adopted in the homogeneous case being somewhat arbitrary because of the mismatch between the true noise model and the one used in the detection.

### C. Impact of the Exposure Time

Figure 8 illustrates the influence of the exposure time on the likelihood maps and on the detection maps for several threshold values. As expected, for 2 h of total exposure time instead of 1, the likelihood map has fewer spurious sidelobes and thresholding is easier. This can be seen in the detection maps: there are fewer false detections for the low threshold of 3 (second line of Fig. 8). Additionally, all planets are detected even for higher threshold values, up to a value of 5 (last line of Fig. 8). The 2 h exposure time thus results in a more reliable detection; in the Gaussian setting assumed here, and assuming that the quasi-static aberrations have been perfectly removed by the image differentiation, a $4\sigma$ detection such as the one obtained on Fig. 7 corresponds to a $6\times10^{-5}$ probability of false alarm, whereas the $5\sigma$ detection of Fig. 8 corresponds to a $6\times10^{-7}$ probability of false alarm.

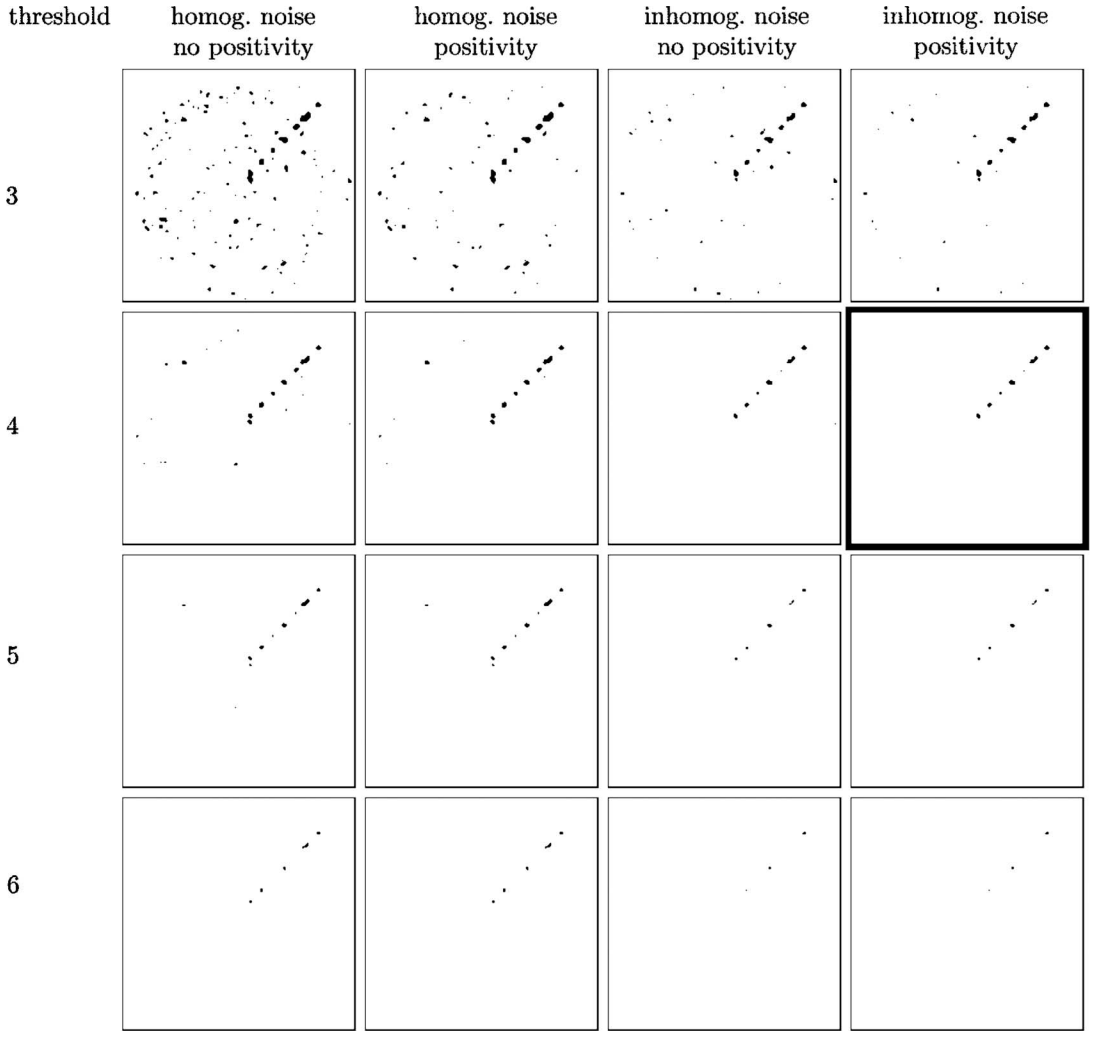


Fig. 7. Detection maps obtained by thresholding the maps of the SNR of the estimated intensity of Fig. 6, for various thresholds mentioned in the left column. From left to right: homogeneous noise, no positivity; homogeneous noise and positivity; inhomogeneous noise, no positivity; inhomogeneous noise and positivity.

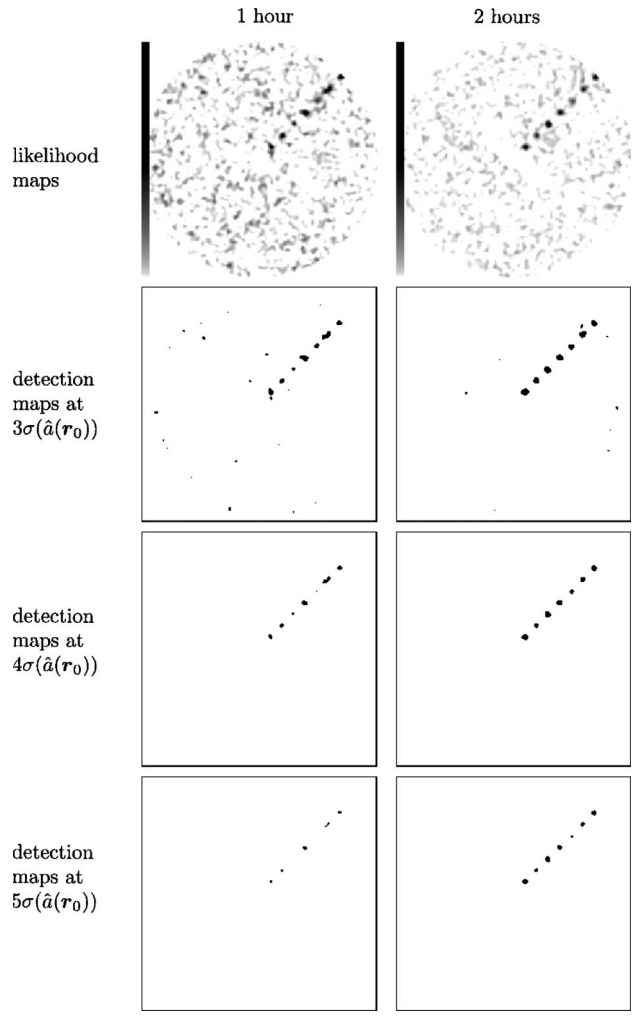


Fig. 8. Likelihood and detection maps for different exposure times: 1 h (left) and 2 h (right) with 100 images in each case. The estimation is done with the inhomogeneous noise model and a positivity constraint.

## 6. DISCUSSION

We have presented a method based on maximum likelihood for exoplanet detection with ground-based instruments such as SPHERE, and tested it by means of simulations. This method makes use of the temporal diversity of the images brought by field rotation in order to disentangle planets from speckles. It can enforce a positivity constraint on the estimated intensity and can use the noise variance map of the images, the beneficial influence of which has been demonstrated. A reasonable detection criterion has also been proposed and tested; it is based on the computation of the noise propagation from the images to the estimated intensity of the potential planet. As an example, under the assumptions and simulation conditions described in the paper, a reliable detection is obtained with 2 h of data for a $10^6$ intensity ratio between the star and the planet.

While the results of our simulations are very encouraging, these simulations should be made more realistic by taking into account the variations of turbulence strength and of static aberrations during the night. The effect of these variations on the images will be partially compensated for by performing a spectral difference between simultaneous image channels and using these spectral difference images as inputs $\boldsymbol{i}_t$ for the method proposed in this paper. Yet, this compensation will be only partial. Preliminary simulations (not presented herein) suggest that the subtraction between images taken at different times must incorporate a scaling factor that can be optimized for each image pair. Additionally, the optimal scaling factor varies with the distance to the star, which suggests performing the detection in different annuli with a potentially different scaling factor for each annulus.

One short-term perspective is thus to assess the performance of the method in the case of slowly evolving aberration and turbulence parameters using both spectral channels of the IRDIS instrument. Additionally, because the pair-wise image combination is quite flexible, this combination should be adapted to the variability of these parameters in order to optimize the detection. Another short-term perspective is to optimize the code in order to reduce the computation time. Additionally, the design of a more elaborate detection criterion taking into account the non-Gaussianity of the noise also deserves further studies. As a final note we mention that this method, which has been named ANDROMEDA, for ANgular Differential OptiMal Exoplanet Detection Algorithm, is likely to be implemented in the data pipeline of the SPHERE/IRDIS instrument, so that it will be available to astronomers for processing the bi-spectral images provided by this instrument.

## ACKNOWLEDGMENTS

The authors thank David Mouillet of Laboratoire d'Astrophysique de l'Observatoire de Grenoble (LAOG) for sharing his expertise on the SPHERE system, and the people from the SPHERE consortium for several fruitful discussions, notably Marcel Carbillet, Anthony Boccaletti, Maud Langlois, Kjetil Dohlen, and Jean-Luc Beuzit.

## REFERENCES

1. J. R. P. Angel, "Groundbased imaging of extrasolar planets using adaptive optics," Nature (London) **368**, 203–207 (1994).
2. A. Burrows and D. Sudarsky, "Models of irradiated extrasolar giant planets," in *Scientific Frontiers in Research on Extrasolar Planets*, Vol. 294 of Astronomical Society of the Pacific Conference Series, D. Deming and S. Seager, eds. (Astronomical Society of the Pacific, 2003), pp. 491–498.
3. J.-L. Beuzit, M. Feldt, K. Dohlen, D. Mouillet, P. Puget, and F. Wildi, "SPHERE: a 'planet finder' instrument for the VLT," Proc. SPIE **7014**, 701418 (2008).
4. B. A. Macintosh, J. R. Graham, D. W. Palmer, R. Doyon, J. Dunn, D. T. Gavel, J. Larkin, B. Oppenheimer, L. Saddlemyer, A. Sivaramakrishnan, J. K. Wallace, B. Bauman, D. A. Erickson, C. Marois, L. A. Poyneer, and R. Soummer, "The Gemini Planet Imager: from science to design to construction," Proc. SPIE **7015**, 701518 (2008).
5. M. R. Swain, G. Vasisht, and G. Tinetti, "The presence of methane in the atmosphere of an extrasolar planet," Nature (London) **452**, 329–331 (2008).
6. T. Fusco, G. Rousset, J.-F. Sauvage, C. Petit, J.-L. Beuzit, K. Dohlen, D. Mouillet, J. Charton, M. Nicolle, M. Kasper, and P. Puget, "High-order adaptive optics requirements for direct detection of extra-solar planets: Application to the

SPHERE instrument," Opt. Express **14**, 7515–7534 (2006).
7. B. Lyot, "The study of the solar corona and prominences without eclipses (George Darwin Lecture, 1939)," Mon. Not. R. Astron. Soc. **99**, 580–594 (1939).
8. D. Rouan, P. Riaud, A. Boccaletti, Y. Clénet, and A. Labeyrie, "The Four-Quadrant Phase-Mask Coronagraph. I. Principle," Publ. Astron. Soc. Pac. **112**, 1479–1486 (2000).
9. R. Soummer, C. Aime, and P. E. Falloon, "Stellar coronagraphy with prolate apodized circular apertures," Astron. Astrophys. **397**, 1161–1172 (2003).
10. R. Racine, G. A. Walker, D. Nadeau, and C. Marois, "Speckle noise and the detection of faint companions," Publ. Astron. Soc. Pac. **112**, 587–594 (1999).
11. C. Marois, R. Doyon, D. Nadeau, R. Racine, and G. A. H. Walker, "Effects of quasi-static aberrations in faint companion searches," in *Astronomy with High-Contrast Imaging*, Vol. 8 of EAS Publications Series, C. Aime and R. Soummer, eds. (EDP Sciences, 2003), pp. 233–243.
12. C. Marois, R. Doyon, D. Nadeau, R. Racine, M. Riopel, P. Vallée, and D. Lafrenière, "TRIDENT: an infrared differential imaging camera optimized for the detection of methanated substellar companions," Publ. Astron. Soc. Pac. **117**, 745–756 (2005).
13. K. Dohlen, M. Langlois, and M. Saisse, "The infrared dual imaging and spectrograph for SPHERE: design and performance," Proc. SPIE **7014**, 70143L (2008).
14. A. Labeyrie, "Detection of extra-solar planets," in *Formation of Planetary Systems*, A. Brahic, ed. (Cepadues-Editions, Toulouse, 1982), pp. 883, 885–888.
15. M. Mueller and G. Weigelt, "High-resolution astronomical imaging by roll deconvolution of space telescope data," Astron. Astrophys. **175**, 312–318 (1987).
16. C. Marois, D. Lafrenière, R. Doyon, B. Macintosh, and D. Nadeau, "Angular differential imaging: A powerful high-contrast imaging technique," Astrophys. J. **641**, 556–564 (2006).
17. D. Lafrenière, C. Marois, R. Doyon, D. Nadeau, and É. Artigau, "A new algorithm for point-spread function subtraction in high-contrast imaging: A demonstration with angular differential imaging," Astrophys. J. **660**, 770–780 (2007).
18. I. Smith, A. Ferrari, and M. Carbillet, "Detection algorithm of exoplanets in field-rotated images: preliminary results on simulated SPHERE coronographic images," in *Semaine de l'Astrophysique Française*, SF2A (EDP Sciences, 2007).
19. I. Smith, M. Carbillet, A. Ferrari, D. Mouillet, A. Boccaletti, and K. Dohlen, "Simulation of moving exoplanets detection using the VLT instrument SPHERE/IRDIS," Proc. SPIE **7015**, 70156F (2008).
20. L. M. Mugnier, J.-F. Sauvage, T. Fusco, and G. Rousset, "Multi-channel planet detection algorithm for angular differential imaging," in *Adaptive Optics: Analysis and Methods*, OSA Technical Digest (OSA, 2007), paper ATu A4.
21. J.-F. Sauvage, L. Mugnier, A. Woelfflé, T. Fusco, and G. Rousset, "Multi-channel algorithm for exoplanets detection by angular differential imaging," in *Semaine de l'Astrophysique Française*, SF2A (EDP Sciences, 2007).
22. L. M. Mugnier, T. Fusco, and J.-M. Conan, "MISTRAL: a myopic edge-preserving image restoration method, with application to astronomical adaptive-optics-corrected long-exposure images," J. Opt. Soc. Am. A **21**, 1841–1854 (2004).
23. L. Jolissaint, J.-P. Véran, and R. Conan, "Analytical modeling of adaptive optics: foundations of the phase spatial power spectrum approach," J. Opt. Soc. Am. A **23**, 382–394 (2006).
24. R. Conan, T. Fusco, G. Rousset, D. Mouillet, J.-L. Beuzit, M. Nicolle, and C. Petit, "Modeling and analysis of XAO systems. Application to VLT-Planet Finder," Proc. SPIE **5490**, pp. 602–608 (2004).
25. J.-F. Sauvage, "Calibration et méthodes d'inversion en imagerie haute dynamique pour la détection directe d'exoplanètes," Ph.D. thesis (Université Paris VII, 2007).